



UNIVERSITY OF LEEDS

This is a repository copy of *Functionalization and densification of inter-bundle interfaces for improvement in electrical and thermal transport of carbon nanotube fibers*.

White Rose Research Online URL for this paper:

<http://eprints.whiterose.ac.uk/102278/>

Version: Accepted Version

---

**Article:**

Qiu, L, Wang, X, Tang, D et al. (6 more authors) (2016) Functionalization and densification of inter-bundle interfaces for improvement in electrical and thermal transport of carbon nanotube fibers. *Carbon*, 105. pp. 248-259. ISSN 0008-6223

<https://doi.org/10.1016/j.carbon.2016.04.043>

---

© 2016. This manuscript version is made available under the CC-BY-NC-ND 4.0 license  
<http://creativecommons.org/licenses/by-nc-nd/4.0/>

**Reuse**

Unless indicated otherwise, fulltext items are protected by copyright with all rights reserved. The copyright exception in section 29 of the Copyright, Designs and Patents Act 1988 allows the making of a single copy solely for the purpose of non-commercial research or private study within the limits of fair dealing. The publisher or other rights-holder may allow further reproduction and re-use of this version - refer to the White Rose Research Online record for this item. Where records identify the publisher as the copyright holder, users can verify any specific terms of use on the publisher's website.

**Takedown**

If you consider content in White Rose Research Online to be in breach of UK law, please notify us by emailing [eprints@whiterose.ac.uk](mailto:eprints@whiterose.ac.uk) including the URL of the record and the reason for the withdrawal request.

# Functionalization and Densification of Inter-Bundle Interfaces for Improvement in Electrical and Thermal Transport of Carbon Nanotube Fibers

Lin Qiu,<sup>ab</sup> Xiaotian Wang,<sup>c</sup> Dawei Tang,<sup>\*a</sup> Xinghua Zheng,<sup>\*ad</sup> Pamela M. Norris,<sup>b</sup> Dongsheng Wen,<sup>e</sup> Jingna Zhao,<sup>f</sup> Xiaohua Zhang,<sup>f</sup> and Qingwen Li<sup>f</sup>

<sup>a</sup>Institute of Engineering Thermophysics, Chinese Academy of Sciences, Beijing, 100190, China

<sup>b</sup>Department of Mechanical and Aerospace Engineering, University of Virginia, Charlottesville, VA 22904-4746, USA

<sup>c</sup>Technical Institute of Physics and Chemistry, Chinese Academy of Sciences, Beijing, 100190, China

<sup>d</sup>Department of Mechanical Engineering, University of California, Riverside, CA 92521, USA

<sup>e</sup>School of Chemical and Process Engineering, University of Leeds, Leeds LS2 9JT, UK

<sup>f</sup>Key Laboratory of Nano-Devices and Applications, Suzhou Institute of Nano-Tech and Nano-Bionics, Chinese Academy of Sciences, Suzhou, 215123, China

**ABSTRACT** Electrical and thermal management in nanodevices by means of carbon nanotube is highly promising. One main challenge toward CNT-based nanoscale electrical and thermal management devices is the development of effective strategies for reducing the bundle-bundle interface resistance. Here we report a novel strategy, based on the densification of CNT bundles

---

\* Corresponding authors. Tel: 86 10 82543022. E-mail: [dwtang@mail.etp.ac.cn](mailto:dwtang@mail.etp.ac.cn) (Dawei Tang), [jzzhengxinghua@163.com](mailto:jzzhengxinghua@163.com) (Xinghua Zheng).

and the functionalization of inter-bundle interfaces for effectively enhanced interfacial electrical and thermal transport. The densification is realized by utilizing the local electrostatic cohesion; and the functionalization is realized by the interface-decorated functional groups. Experiments and theoretical analysis demonstrated obviously enhanced interfacial electrical and thermal conductance originates from: (1) local Coulomb electrostatic cohesion between CNT bundles due to surface-induced dipole moments. This effect can promote both electrical and thermal conductance nearly 2.8 times higher than non-functionalized counterpart. (2) Increased interfacial electron transport channels and thermal vibrations due to surface-decorated functional groups. This effect can bring about up to 75% and 95% improvement for thermal and electrical conductance, respectively. This study provides a new methodology for programmable operation of electrical and thermal properties at inter-bundle interfaces and guidance for design of CNT-based electrical and thermal management devices.

## 1. Introduction

Nanoscale electrical and thermal transport are essential to the performance of many up-to-date key devices such as phase change memory devices, heat assisted magnetic recording, thermal management of high power and nanoscale electronic and optoelectronic devices, and delivery vehicles for molecules in medical therapies and next-generation long distance electricity transport wires [[1]-[4]]. Carbon nanotubes (CNTs) have always attracted intensive interest in the above-mentioned applications due to their excellent thermal and electrical properties [[5]-[10]]. Owing to extremely long mean free path (MFP) and ballistic transport nature, the electrical and thermal conductivities of individual CNT have very high theoretical values [[11]-[14]]. In order to investigate the electrical conductivities of CNTs, four-probe technique [[15]-[18]], was

first applied to measure axial electrical conductivities ( $\sigma$ ) of individual single-wall CNT (SWCNT) and multiwall CNT (MWCNT), rendering rivalled ( $10^6$  S/m for MWCNTs) [[15]-[16]] or even better results ( $10^8$  S/m for SWCNTs) [[17]-[18]] compared to the best electrical conductor copper ( $6 \times 10^7$  S/m) at room temperature (RT). Multiple experimental techniques were successfully applied to thermal characterization in succession [[19]-[23]]. The obtained axial thermal conductivities ( $\kappa$ ) of individual SWCNTs and MWCNTs also demonstrate competitive values, i.e.  $\sim 600$ - $3000$  W/mK for SWCNTs (range generally attributed to thermal contact resistance and uncertainty in diameter determination) and  $\sim 40$ - $3000$  W/mK for MWCNTs (range generally attributed to differences in defect concentration arising from the different synthesis methods) [[24]], rivaling the up-to-date best thermal conductor diamond (3000 W/mK). For practical applications, CNTs need to be assembled into macroscopic architectures; however the bulk electrical and thermal conductivities of CNT ensembles were found much lower than the individual values. A typical example is the CNT spun fiber, whose axial electrical conductivity is experimentally verified within the range  $10^4 \sim 10^5$  S/m [[25], [26]] and thermal conductivity is barely  $30 \sim 380$  W/mK [[6], [27],[28]]. These one order of magnitude reductions in both electrical and thermal conductivities clearly retard efficient applications of CNTs. It was also reported that for light weighted high conductive CNT fiber, which is designed for fulfilling European Space Agency's stringent space thermal control requirement in all phases of a space mission, the heat accumulation effect could raise the fiber temperature up to over 500 °C, leading to self-ignition that is more dangerous than the “blow out” of conventional metal wires [[29]]. Therefore, endeavor toward developing CNT fibers with remarkably improved electrical and thermal transport is urgently needed for future applications in relevant energy conservation and conversion, information technology and thermal management systems.

Generally, two culprits have been identified responsible for the reduced electrical and thermal conductivities at the bulk scale: inter-tube interface contact resistance, and high impurity content. Firstly, inter-tube contact within CNT fibers (CNTFs) induces large interfacial resistance, which is verified to be the main barriers for electron and phonon transport as it works as scattering sites for energy carries [[30], [31]]. Secondly, the existence of impurities, such as amorphous carbon and catalytic particles, causes significant scattering, reducing both  $\sigma$  and  $\kappa$ . Since impurities also inevitably exist for most CNT fabrication methods even after post-treatment, such as catalytic chemical vapour deposition (CVD), improving inter-bundle interface contact resistance is regarded as the most practical and effective approach to leverage overall electrical and thermal transport in CNTFs. Typically, poor inter-tube interfacial contact in CNTFs appreciably stem from large inter-bundle separation, which not only impedes interfacial transferring of electrons for electrical transport, but also weakens interfacial interaction of phonons for thermal transport. Therefore, modifying interfaces to break the limit of existing inter-tube spacing is supposed to be a rational solution to enhance interfacial electrical and thermal conduction. Some pioneering endeavours of ours [[32]-[36]] and others [[26], [30], [32], [37]-[40]] discovered that physical and chemical manipulations, specifically liquid infiltration into the internal spaces between contiguous bundles and bridging the interface with short covalently bonding molecules, respectively, could effectively improve the inter-bundle contact, resulting in significant increase in mechanical properties, such as the tensile strength. However, to the best of our knowledge, these manipulating mechanisms in inter-bundle interface have never been applied for the in-depth electrical and thermal design of efficient CNT assemblies, let alone quantitative tuning of electrical and thermal performance, which is highly anticipated for smart CNT assembly for future efficient energy system.

Motivated thus, we demonstrate a promising strategy that engineering the electrical and thermal transports in CNT fibers through programmable modulations the inter-bundle interface contact of CNTs. The exquisitely programming scheme is based on two engineering manipulation mechanisms, the densification of CNT bundles and the functionalization of inter-bundle interfaces. The results showed that a synergistic effect of densification and functionalization of CNTs can effectively enhance the electrical and thermal conductivities of CNTFs. Significantly, the mechanism of improved inter-bundle electrical and thermal conductance are studied in detail. Multiple experimental characterization techniques and theoretical model description are performed for understanding the improvement of inter-bundle interface contacts: (1) Densification of CNTs via polar solvents can decorate dipoles on the surface of CNTs, which will provide strong local Coulomb electrostatic cohesion between neighboring CNT bundles. It was found that this step can enhance both the electrical and thermal conductance nearly 2.8 times than non-densified counterpart. (2) The functional groups (FGs) modified on the surface of CNTs can serve as electron relays and channels to facilitate the inter-bundle charge transport. Also, the FGs can form stronger inter-bundle interactions than the van der Waals forces, which can further improve the interfacial thermal vibrations. It was found that this step can obtain up to 75% and 95% enhancement in thermal and electrical contact conductance, respectively. The progress made so far will guide further development in structure design of CNT-based nanoscale electrical and thermal management devices, in addition to fueling the exploration of such materials for high-performance nanodevices in energy conservation and conversion, information technology and medical therapy.

## 2. Fabrication and characterizations

## 2.1 Sample Preparation

Four densification and functionalization schemes for modifying inter-bundle interfaces were conceived and applied to the raw CNTFs spun out from CVD-grown identical vertically-aligned CNT arrays, which were mainly 2-3 walled and  $\leq 6$  nm in diameter [[32]]. A detailed description of the fabrication process can be found in previous publications of some of the co-authors [[32]], [34], [35]]. Briefly, an infiltration process was set up at the end of the identical CNT sheet pulled out of the as-grown array. By drawing and twisting under the optimal spin condition, a long and uniform fiber with diameter  $\sim 10$   $\mu\text{m}$  and twist angle  $< 12^\circ$  was obtained [[32]]. The first sample for densification manipulation was infiltration (I) using a polar protic solvent ethanol (E) to induce internal structure variation occurrence of local densification between CNT bundles, as shown in Fig. 1. It is believed that both local dipole moments transferred from polar solvents to CNTs and the capillary force during the evaporation of polar solvents contribute to the occurrence of CNT densification [[32], [33], [37]]. The ensuing sample is denoted as CNTF-E-I. The second sample was also infiltration but replacing ethanol with ethylene glycol (EG), whose double highly polar OH groups resulted in more dipole- $\pi$  interactions. This sample is similarly denoted as CNTF-EG-I. The third and fourth samples employed a two-stage manipulation approach. The first stage was infiltration for forming local densification of CNT bundles and the second stage was acidization (A) for introducing covalent bonding linkers, typically short functional groups, to CNT sidewalls and ends (Fig. 1). The third sample used ethanol as infiltration solvent and concentrated nitric acid ( $\text{HNO}_3$ , 16M) as acidization solvent. This sample is therefore denoted as CNTF-E-I-A. The fourth sample was similar to the third one except that ethylene glycol was used to replace ethanol during the first infiltration process. And this sample is accordingly denoted as CNTF-EG-I-A.

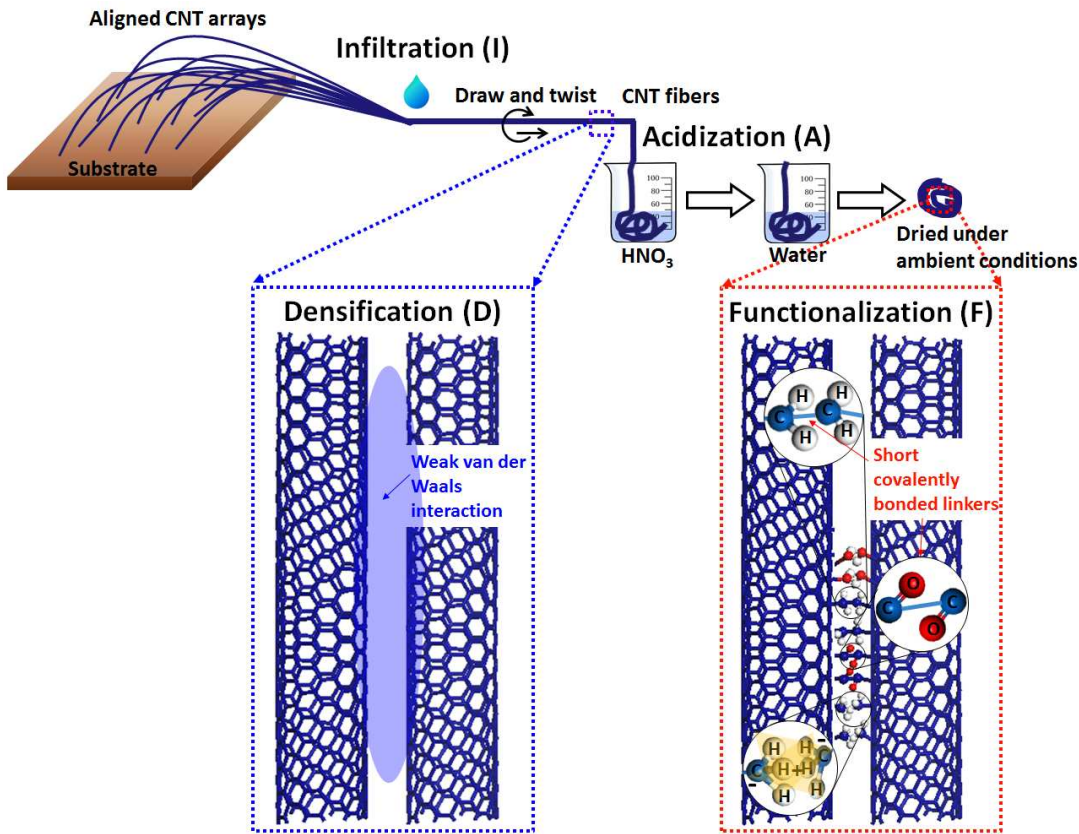


**Fig. 1.** Schematic diagram showing the fabrication of condensed and functionalized CNT fibers. A continuous and uniform CNT sheet is drawn under twisting to from the fiber. Two-stage manipulations: in the first-stage, abundant local densifications of bundles were formed through physical infiltration, drawing and twisting; in the second-stage, short covalently bonding linkers were introduced through chemical acidization. Inserts: inter-tube interactions for the two stages of manipulations. Van der Waals forces and weaker Coulomb electrostatic interaction induced by dipole moments of highly polar solvents coexist for the infiltration-treated sample (blue dotted box, CNTF-E-I and CNTF-EG-I); and additional chemical bonding linkers will exist after acidizing the infiltration-treated samples (red dotted box, CNTF-E-I-A and CNTF-EG-I-A). Four types of short covalently bonding linker molecules ( $-\text{OH}$  /  $-\text{CH}_2-$  /  $-\text{CH}_3$  /  $-\text{C=O}$ ) are formed on CNT bundles surface.

## 2.2 Analysis of Covalently Bonded Linkers

Our FT-IR experimental results showed four types of functional groups were successfully decorated on the surface of CNTs after the HNO<sub>3</sub> acidization: hydroxyl (–OH), methyl (–CH<sub>3</sub>) / methylene(–CH<sub>2</sub>–), carbonyl (–C=O) [[35]]. Furthermore, the concentration of oxygen atoms within functional groups for two acidized samples, i.e., CNTF-E-I-A and CNTF-EG-I-A, was analyzed by using X-ray photoelectron spectroscopy (XPS), which was performed on the Thermo Scientific ESCALab 250Xi using 200 W monochromated Al K $\alpha$  radiation. The 500  $\mu\text{m}$  X-ray spot was used for XPS analysis. The base pressure in the analysis chamber was about  $3 \times 10^{-10}$  mbar. Typically the hydrocarbon C1s line at 284.8 eV from adventitious carbon was used for energy referencing.

[Fig. 2](#) demonstrates the XPS analysis results. It is observed that an appreciably increasing intensity of O1s peak for the chemical acidization group ([Fig. 2C](#) and [Fig. 2D](#)) compared with the physical infiltration group ([Fig. 2A](#) and [2B](#)). The remarkable growth of oxygen atoms (from ~6% to ~15%) together with attenuation of carbon atoms (from ~90% to ~78% ) after HNO<sub>3</sub> acidization demonstrated that oxygen-containing functional groups were successfully introduced to carbon atoms.

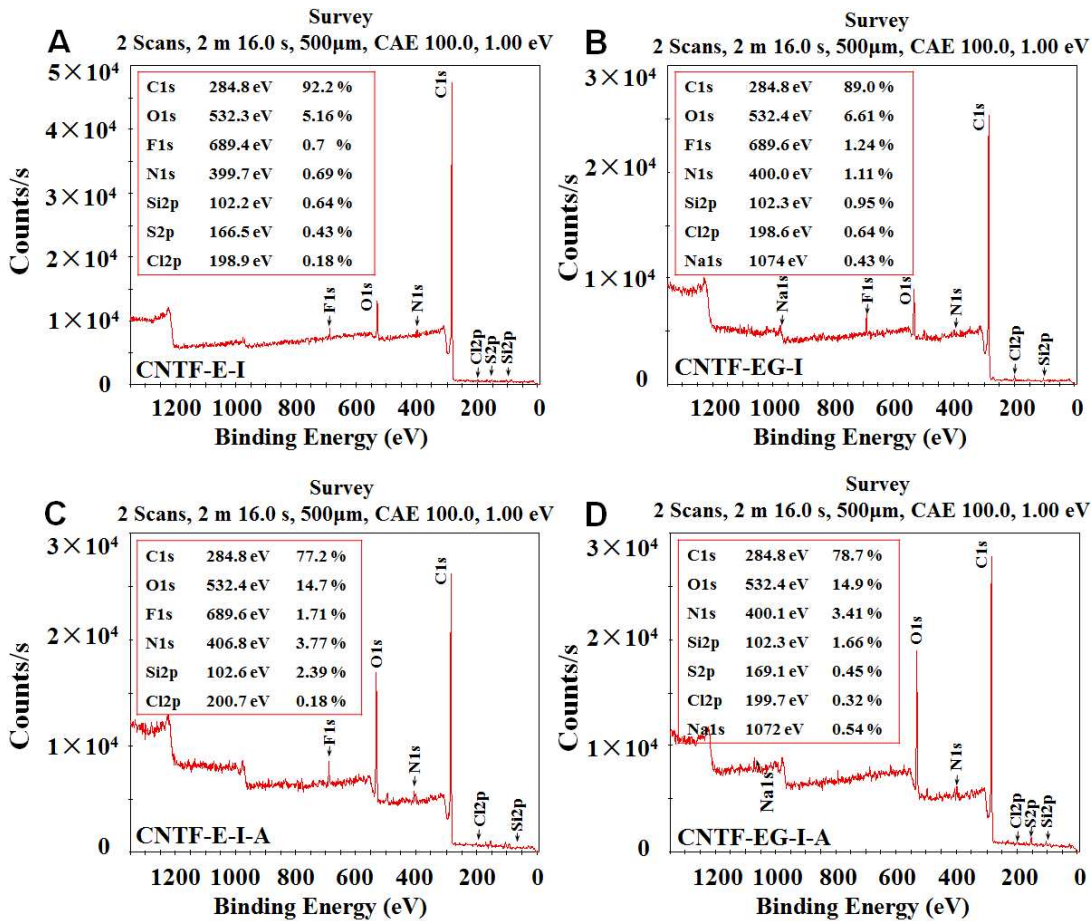


**Fig. 2. XPS spectra of (A) CNTF-E-I, (B) CNTF-EG-I, (C) CNTF-E-I-A, and (D) CNTF-EG-I-A.**

**Inserts:** peak position and atomic fraction of each element. The successful introduction of oxygen-containing functional groups is confirmed by attenuated C fraction and growth of O fraction.

### 2.3 Microscopic Structure Parameters Characterization

The surface morphology of the four CNTFs studied was obtained from a HITACHI S-4300 field-emission scanning electron microscope (FESEM) and their diameters were also measured by using this apparatus. It can be clearly seen that acidization typically induced remarkable rough surface compared with that only treated by infiltration with polar solvents (see Fig. 3).

FESEM analysis shows the diameters of CNTFs are in the range from ~ 10.7 to 9.3 μm, as shown in Table 1. The fiber diameter decreased slightly by ~0.5 μm after ethylene glycol

infiltration instead of ethanol and by  $\sim 1 \mu\text{m}$  after the acidization, which suggested that there were distinguishable local densification degree for the two polar protic solvents and stronger inter-tube interaction than van der Waals forces after acidization. Owing to the thickness non-uniformity, an average value among several locations was used in the diameter analysis. The length of each sample was also determined by FESEM. Moreover, we present side-view FESEM of the four CNTF samples where the surface morphology and densification degree can be easily distinguished. CNTF-E-I shows large tube waviness (Fig. 3A) inherited from the as-spun fiber owing to the rapid vaporization of ethanol. In contrast, CNTF-EG-I demonstrates greatly reduced tube waviness (Fig. 3B) owing to much lower evaporation rate and higher polarity of ethylene glycol. Additional acidization manipulation using concentrated nitric acid had remarkable influence on CNT surface structure. Specifically, multiple functional groups are introduced and thus induce remarkably rough surface for CNTF-E-I-A and CNTF-EG-I-A (Fig. 3C, D). High-magnification image shows that the CNTs in ethanol infiltrated samples, i.e., CNTF-E-I and CNTF-E-I-A, are drawn closer at different places to form small and localized densification and tiny holes, which makes the global densification difficult, as shown in Insert in Fig. 3C. Slightly larger bundles together with large empty rooms are formed within ethylene glycol infiltrated samples, CNTF-EG-I and CNTF-EG-I-A, as shown in Insert in Fig. 3D. Statistical distributions of bundle diameter for those two category of fibers demonstrate distinguishable bundle sizes, i.e., an individual tube performs as a unit or 2 of them aggregate to form a bundle for ethanol infiltrated fibers and approximately 3 tubes form a bundle for ethylene glycol infiltrated fibers (Fig. 3E,F). These structure variations suggest stronger dipole moment in physical infiltration manipulation could form larger CNT bundles, resulting in an increase of inter-bundle contact area and thus enhanced interface conductance [[24]].

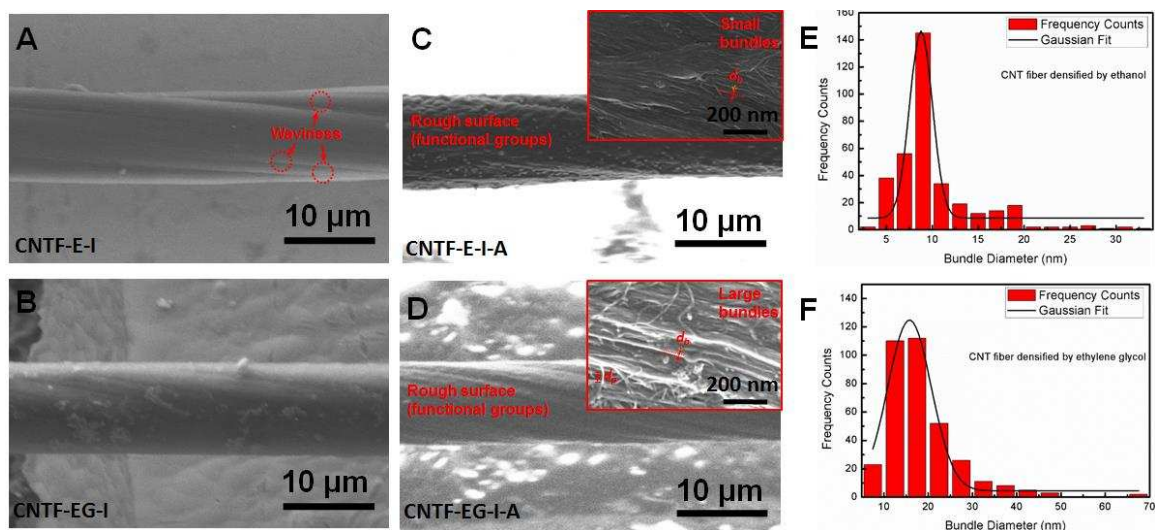


**Fig. 3. Real surface morphology for (A) ethanol infiltrated sample (CNTF-E-I), (B) ethylene glycol infiltrated sample (CNTF-EG-I), (C) ethanol infiltrated + HNO<sub>3</sub> acidized sample (CNTF-E-I-A), and (D) ethylene glycol infiltrated + HNO<sub>3</sub> acidized sample (CNTF-EG-I-A). Inserts: high-magnification images showing the microscopic bundle diameter and orientation for ethanol infiltrated and ethylene glycol infiltrated samples. (E) and (F) are statistical distributions of bundle diameters for ethanol and ethylene glycol treated fibers, respectively.**

**Table 1 Selected properties of functionalized CNT fibers. Their structural parameters determined by SEM (diameter D), XRD (interlayer spacing d<sub>002</sub> and out-of-plane coherence length L<sub>c</sub>) and Raman spectroscopy (length of ideal graphene layers fringes L<sub>1</sub>), the electrical conductivity σ by four-probe method, the apparent thermal conductivity κ<sub>ap</sub> and thermal diffusivity α<sub>ap</sub> measured by the self-heating 3ω method, and lattice thermal conductivity κ<sub>L</sub> by deducting the electron contribution according to Wiedemann-Franz law.**

Sample	D	L <sub>1</sub>	L <sub>c</sub>	d <sub>002</sub>	α <sub>ap</sub>	κ <sub>ap</sub>	κ <sub>L</sub>	σ
	[μm]	[nm]	[nm]	[Å]	[mm <sup>2</sup> /s]	[W/mK]	[W/mK]	[S/cm]

CNTF-E-I	10.7	6.1	1.2	3.512	$19+0.208L^2$	$21.2+0.214L^2$	21.0	243
CNTF-EG-I	10.2	5.9	1.3	3.606	$26+0.219L^2$	$30.5+0.224L^2$	30.3	309
CNTF-E-I-A	9.9	6.0	1.2	3.597	$34+0.225L^2$	$37.2+0.231L^2$	36.8	450
CNTF-EG-I-A	9.3	5.8	1.2	3.610	$47+0.240L^2$	$51.0+0.246L^2$	50.5	659

Two important microscopic structural parameters, the interlayer spacing  $d_{002}$  and the out-of-plane coherence length  $L_c$  were determined by using a Bruker D8 Focus polycrystal X-ray diffractometer. The CNT fiber samples were first pulverized in an agate mortar and pestle, and then pass through a 150 mesh standard sieve. After well mixed with 10-20 mass % standard silicon in the agate mortar, the mixture was homogeneously packed into a hole of 0.2 mm in depth on a glass holder. CuKa X-ray was used, where CuKb was Ni-filtered. The accelerating voltage and current applied to the X-ray tube was set to be 40 kV and 40 mA. A step-scanning with 0.02° interval was used to obtain the diffraction profile. The operations strictly follow the specification for a standard procedure of X-ray diffraction (XRD) measurements on carbon materials [41].  $d_{002}$  was determined from the diffraction angle of the carbon (002) reflection, while  $L_c$  was calculated from the full width at half maximum (FWHM) of the (002) reflection (see Fig. 4).

Representative XRD graphs of the four functionally manipulated CNT fibers are shown in Fig. 4A, B. To ensure an accurate and reliable result, the diffraction angle of the silicon standard and the angle displacement  $\delta_{Si-C}$  between silicon and CNT fiber powder were used to correct the diffraction angle of CNT fiber [41]. The values of interlayer spacing  $d_{002}$  were then calculated from Bragg's law [41] using the corrected diffraction angle of carbon nanotube fibers. Since there is no clear separation in the (002) reflection for the carbon and the (111) reflection for the silicon standard from the experimental observation, each reflection needs to be resolved into two

separated peaks for K $\alpha$ 1 and K $\alpha$ 2 and to get the full width at half maximum (FWHM) of the K $\alpha$ 1 peak for both carbon B and silicon standard b. The B and b values can be calculated by  $B_0$  and  $b_0$  combined with the observed FWHMs of the carbon and silicon standard in an unresolved profile [[41]] (shown in Fig. 4). The height of crystalline L<sub>c</sub> was then calculated from the true FWHM,  $\beta$  of the (002) reflections ( $\beta$  is calculated by B and b) using the Scherrer equation [[41], [42]] by an analysis software, MDI jade. The values of d<sub>002</sub> for the four fibers are around 3.6 Å, consistent with both the theoretically predicated and experimentally obtained values for MWCNT in other literatures [43], [44]. Significantly, the L<sub>c</sub> values for all four fibers are around 1.2 nm (listed in Table 1), agreeing well the average three-walled structural feature of CNTs. This result suggests that both densification and functionalization processes would not change the wall spacing or wall number within a CNT, which means the thermal conductivity of an individual CNT would not be changed appreciably after densification and functionalization. Therefore, any difference in electrical and thermal transport induced by using the proposed treatment approaches, i.e., densification and functionalization, is only attributed to the variation of the inter-bundle electrical and thermal conductance.

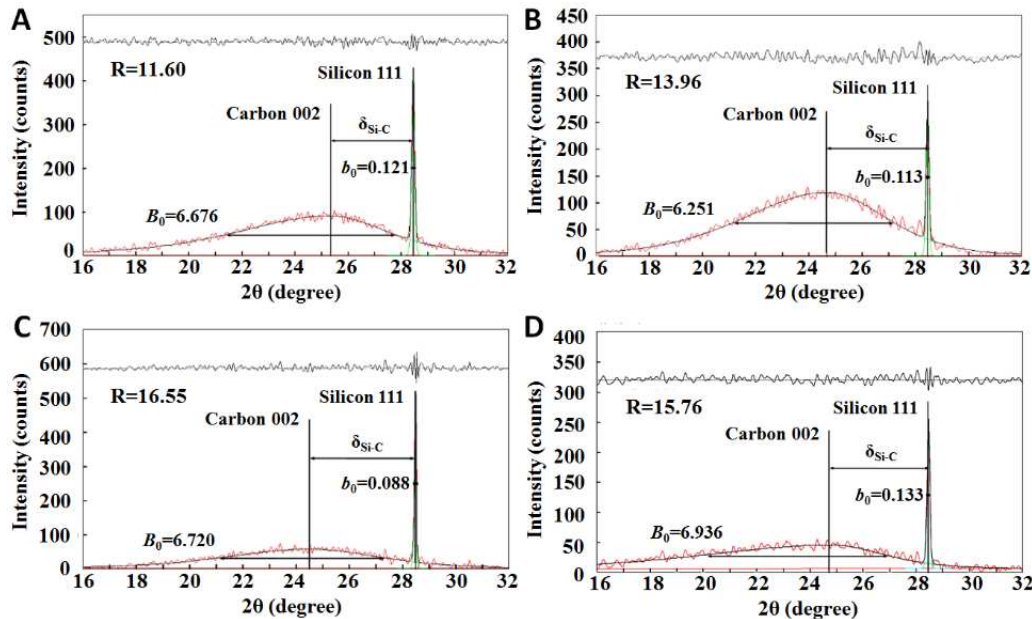


**Fig. 4. XRD spectra of the four functionalized carbon nanotube fibers with standard silicon powder for characterizing  $L_c$  and  $d_{002}$  by a profile fitting procedure. (A), (B), (C) and (D) corresponds to CNTF-E-I, CNTF-EG-I, CNTF-E-I-A and CNTF-EG-I-A, respectively.**

As the CNT fiber presented relatively low crystallization, which makes it difficult to obtain accurate values of another important nanoscale structure parameter, i.e., the average length of ideal graphene layers fringes  $L_1$  from XRD measurement, which is the maximum length before the graphene shells constituting multi-wall CNTs start to distort, Raman spectrometry was considered as the proper tool to determine  $L_1$  [45]-[47]. Unlike using CNT powders for XRD, we used complete individual CNT fibers attached to the silicon wafer with their both ends fixated by conductive silver paint to perform Raman spectroscopy characterization. Raman spectra were collected using a Renishaw Raman system, inVia-ReflexTM with an excitation laser wave-length of 532 nm, an excitation intensity of 5 mW, and a data acquisition time of 10 s. The laser beam was focused to a spot of 1~2  $\mu\text{m}$  approximately in diameter by a 50 $\times$  microscope objective. The Raman band of silicon wafer at 520  $\text{cm}^{-1}$  was used to calibrate the spectrometer.

The Raman spectra obtained are presented in Fig. 5A. Two typical peaks, D (defect) peak and G (graphite) peak were shown and no splitting was observed for them. The G peak at about 1592  $\text{cm}^{-1}$  just represents  $\text{G}^+$  component which is associated with carbon atom vibration along the nanotube axis (LO phonon mode) and its frequency is sensitive to doping induced charge transfer. The G peak positions for our functionalized samples were not shifted appreciably, which suggested no phonon stiffening or softening effect were introduced during the infiltration and acidization processes. The D peak at approximately 1347  $\text{cm}^{-1}$  which is indicative of defects in the CNT samples did not shift appreciably after moderate acidization, which manifested the extra defect concentration introduced via moderate acidization was negligible and thus probably

would not markedly induce electron and phonon scattering which is the culprit for reducing electrical and thermal transport. Generally, the ratio of the intensities of the two Raman peaks at D-band and G-band ( $I_D/I_G$ ) is given as a quasi-quantitative assessment of quality of CNT samples. According to the results reported by Tuinstra and Koenig [46] and Matthews, et al. [47] for polycrystalline graphite, the ratio  $I_D/I_G$  scaled linearly with  $1/L_1$ . Therefore, based on their empirical linear relationship between  $I_D/I_G$  and  $1/L_1$  (see Fig. 5B), the values of  $L_1$  were deduced to be  $\sim 6$  nm (Table 1). Since all the samples for Raman characterization remain their original shape and structure, the obtained values of  $L_1$  reflect the magnitude of average contact length of contiguous CNTs within the CNT fibers. The negligible variations of  $L_1$  after densification and functionalization suggest that lengthwise bundle contact structure does not change appreciably for the present treatment scheme. And thus any changes in the inter-bundle electrical and thermal conductance is only attributed to variations in inter-bundle spacing and additional pathways.

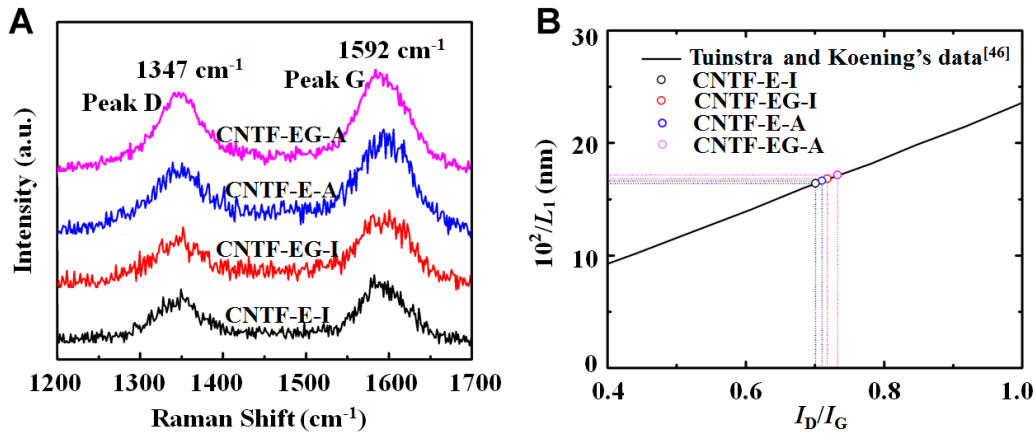


**Fig. 5. (A) Raman spectra of the four CNT fibers with manipulated inter-bundle contact interface, (B) relation between the ratio  $I_{1355}/I_{1575}$  and the  $1/L_1$  values given by Tuinstra and Koenig [46] (solid line) and by the present experiment (open circles).**

## 2.4 Electrical and Thermal Conductivity Measurement

For electrical and thermal characterization, the individual functionalized CNT fiber was suspended on four parallel Cu pads laid out on a printed board [36]. The Cu pads and the printed board served as a heat sink for the fiber specimen during the measurement. The contact resistance between the fiber and Cu pads caused by silver paste bonding is estimated < 8.3% of the total resistance [36] which would not ruin the confidence of the measured electrical and thermal conductivity of the fiber. The electrical conductivities of the CNT fibers were measured by using a four-probe resistivity meter. A current of  $\sim 3 \mu\text{A}$  was introduced into the fiber via two outside Cu pads and the voltage of the in-between part of the fiber was extracted through its connection with two inside Cu pads using a voltmeter. The electrical conductivity was then calculated using the definition  $\sigma = I/RS$ . The length of the in-between part of the fiber l and the cross-section area S were measured according to the FESEM images. To avoid irreversibility caused by dopant desorption during temperature elevation [48], alternate heating and cooling cycling measurements were performed and the reported values were relatively stable values after two or three cycles.

The thermal transport measurement was performed using the self-heating  $3\omega$  technique (Fig. 6), which is believed suitable for one-dimensional conductive wire with the diffusive nature of electronic conductivity [49]-[51]. This is a direct frequency domain quasi-steady-state measurement technique, which can determine thermal conductivity and thermal diffusivity simultaneously. In this technique, the individual fiber is used as the heater and thermometer to determine its average temperature rise. Unlike electrical measurement, considering the length-dependent radiation heat loss, a set of samples with various lengths within 0.5~20 mm from identical CNT fibers were detected for studying the length dependence of thermal transport. The  $3\omega$  experimental apparatus includes a signal generator (Agilent model 33220A), a commercial

lock-in amplifier (Ametek Signal Recovery 7265), a control electrical circuit mounted with Power Amplifier (EG & G Model 5113), an operational amplifier (AMP03), low temperature drift resistors  $R_1 \sim R_8$  (5 PPM/ $^{\circ}\text{C}$ ) and a Model SYN-35-D15A power supply. The voltages between the two inner contact points at different current frequencies were recorded by the lock-in amplifier. The first and third harmonic components were used to deduce thermal properties. During the measurement, the whole test structure was put into a vacuum chamber to remove the convection influence. An alternating current  $I_0 \sin \omega t$  was applied through the two outside pads, inducing a modulated temperature rise of the suspended in-between part of the fiber at an angular frequency of  $2\omega$ , which further resulted in a  $2\omega$  modulated electrical resistance, and finally created a third-harmonic response between the two inside pads,  $U_{3\omega}$  [49]:

$$U_{3\omega} = \frac{4I_{\text{rms}}^3 L R_0^2 \alpha_{\text{CR}}}{\pi^4 S \kappa_{\text{ap}} \sqrt{1 + \tan^2 \varphi}} \quad (1)$$

$$\tan \varphi = \frac{4 f L^2}{\pi \alpha_{\text{ap}}} \quad (2)$$

where the subscript rms corresponds to the effective value,  $U_{3\omega}$  is the amplitude of the third harmonics,  $L$  is the length of the in-between part of the fiber,  $\kappa_{\text{ap}}$  is the apparent thermal conductivity in the axial direction,  $S$  is the cross section area,  $\alpha_{\text{CR}}$  is the temperature coefficient of resistance (TCR) of the fiber,  $f$  is the frequency of the alternating current,  $\varphi$  is the phase angle of the third harmonic voltage, and  $\alpha_{\text{ap}}$  is the apparent thermal diffusivity.

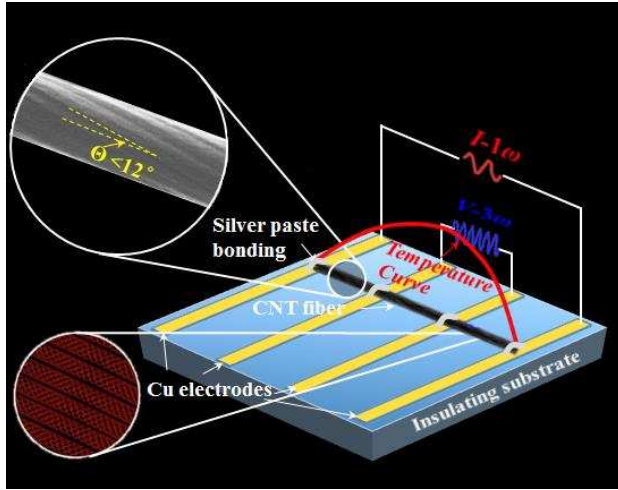


**Fig. 6. Self-heating  $3\omega$  thermal characterization for a single functionalized CNT fiber.** The rendering illustrates that four Cu electrodes are typically deposited on the top surface of an insulating substrate. The CNT fiber is carefully bonded with silver paste on the Cu electrodes to insure suspended structure. Both insulating substrate and Cu electrodes serve as heat sink.

### 3. Results and discussion

#### 3.1 Temperature-programmed electrical transport

The electrical conduction of non-condensed and non-functionalized CNTF has been revealed for the case at low temperature, which verifies a three-dimensional (3D) variable range hopping (VRH) mechanism ( $\sigma \sim T^{-1/4}$ ) dominantly control the electrical transport behaviour for CNT fiber owing to the extremely localized charge carriers stemming from the small cluster size. [[52], [53]] However, the direct 3D VRH formula is not applicable to the condensed and functionalized CNTF near RT zone as the slope of electrical conductivity curves becomes rather small. Fig. 7 shows experimentally obtained electrical conductivity versus temperature  $\sigma(T)$  for the four fibers investigated within the 258~343 K temperature range. Before chemical acidization manipulation, electrical transport of two physical infiltration manipulated fibers demonstrates typical semiconductor characteristics as  $\sigma(T)$  increases with increasing temperature, as shown in

[Fig. 7A](#). HNO<sub>3</sub> acidization leads to dramatic increase in  $\sigma(T)$  at all T and stronger temperature dependence below a transition temperature ( $T^*$ ) and changes to metal-like behaviour  $d\sigma/dT < 0$ , as shown in [Fig. 7B](#). For the physically densified samples, i.e. CNTF-E-I and CNTF-EG-I, electrical transport is primarily controlled by thermal fluctuation induced tunnelling (FIT) [[54], [55]], which was elaborated for incoherent charge transport between long conducting pathways (or large conducting regions) separated by small insulating barriers. In this theory, at small bias voltage, i.e. the ohmic I-V regime, the electrical conductivity is quantitatively described as [[54]-[56]]:

$$\sigma = \sigma_0 \exp\left(-\frac{T_1}{T + T_0}\right) \quad (3)$$

where

$$T_1 = \frac{8\epsilon_r \epsilon_0 A V_0^2}{e^2 k_B w} \quad (4)$$

and

$$T_0 = \frac{16\epsilon_r \epsilon_0 \hbar A V_0^{3/2}}{\pi e^2 k_B (2m_e)^{1/2} w^2} \quad (5)$$

where  $V_0$  is the effective barrier height,  $w$  is the barrier width,  $\epsilon_0$  is the vacuum permittivity,  $\epsilon_r$  is the dielectric constant of the barrier (for air,  $\epsilon_r = 1.00059$ ).  $\hbar$  is the reduced Planck constant, and  $m$  is the electronic mass.  $T_1$  represents the energy required for an electron to cross the barrier between conductive clusters and  $T_0$  is the temperature below which the fluctuation effects become insignificant. First,  $\ln\sigma_0$  was independently obtained from a linear fit based on the  $\ln\sigma \sim 1/T$  data. Then  $T_1$  and  $T_0$  were simultaneously extracted from a least-square fitting based on  $\sigma \sim T$  data and the previously obtained  $\sigma_0$  value [[57]]. The fitted parameters are presented in [Fig. 7A](#) for the CNTF-E-I and CNTF-EG-I. The values of  $T_1$  and  $T_0$  are consistent with literature values

[[57]], but both especially  $T_0$  have significant uncertainties. The decreased  $T_1$  of CNTF-EG-I compared with that of CNTF-E-I is believed to be a result of the increased FIT probability by further densification. For additional  $\text{HNO}_3$  acidized fibers, i.e. CNTF-E-I-A and CNTF-EG-I-A, the transition behaviour to  $d\sigma/dT < 0$  as mentioned previously is straightforwardly assigned to the onset of thermal desorption of functional molecular linkers instead of metallic transition [[57]]. The decisive effect of temperature-induced thermal fluctuation on the success probability of electron tunneling suggests a temperature programmed RT electrical conductivity could be realized for our CNT fibers.

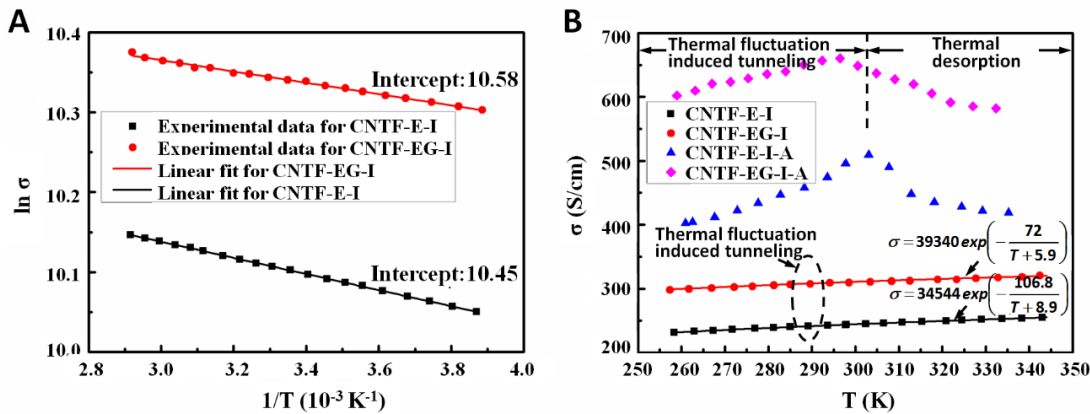


**Fig. 7. Experimental  $\ln\sigma$  versus  $1/T$  data for CNTF-E-I and CNTF-EG-I, (B) Temperature dependence of electrical conductivity for the four densified and functionalized fibers.**

### 3.2 Nanostructure-programmed electrical/thermal transport

The measured RT apparent thermal conductivity and thermal diffusivity for the CNT fibers with different inter-bundle interfaces using  $3\omega$  technique is shown in Fig. 8. The measurement uncertainty in thermal conductivity and thermal diffusivity of an individual carbon fiber is estimated within 12.2% and 8.8% [[36]]. There are a few interesting points to note. First, in contrast to electrical conductivity, it is observed that the measured thermal conductivities of long specimens are much higher than those of short ones and become saturated at a distance below 2

mm. The thermal diffusivity shares the same trend. This phenomenon is consistent with that observed in MWCNT sheet by Aliev, et al. [[27], [50]] It is believed that the distance dependence is attributed to the radial heat loss through thermal radiation, and the apparent thermal conductivity under vacuum condition can be quantitatively expressed as [[27], [50], [51]]:

$$\lambda_{ap} = \lambda_c + \frac{16\epsilon\sigma_0 T_0^3 L^2}{\pi^2 D} \quad (6)$$

$$\alpha_{ap} = \alpha_c + \frac{16\epsilon\sigma_0 T_0^3 L^2}{\pi^2 D \rho C_p} \quad (7)$$

where  $\sigma_0 = 5.67 \times 10^{-8}$  W/m<sup>2</sup>K<sup>4</sup> is the Stefan-Boltzmann constant,  $\epsilon$  is the emissivity,  $D$  is the average diameter of individual one-dimensional heat channels, and  $T_0 = 292$  K is the environment temperature. For porous carbon material the black body emissivity of  $\epsilon = 1$  is used. The solid lines in Fig. 8A, B show very good agreement of the radial loss contribution predicted by Eqs. (6) and (7) with the measured experimental data. The fitting parameters are shown in Table 1 and yield the average diameter of individual one-dimensional heat channels,  $D \approx 9\text{--}10$  μm. This value is surprisingly close to the fiber diameter we found from the FESEM statistical analysis. Nevertheless, the specific heat deduced from the measured  $\lambda$  and  $\alpha$  using  $C_p = \lambda/\rho\alpha$  is insensitive to the radial heat loss (Fig. 8A), which yields the value of  $C_p = 760$  J/kgK. This value is consistent with the reported result from other researchers [[51], [57]]. According to the Wiedemann-Franz law [[42], [57]], the electronic contribution to the RT thermal conductivity is estimated to be 0.2, 0.2, 0.4 and 0.5 W/mK for our fibers, which is much smaller than the measured value. This verifies that it is the phonon rather than the electron that dominates the heat conduction in these fibers. By deducting the electronic contribution from the measured thermal conductivity, the phonon contribution or called lattice thermal conductivity ( $\lambda_L$ ) is obtained, shown in Table 1.

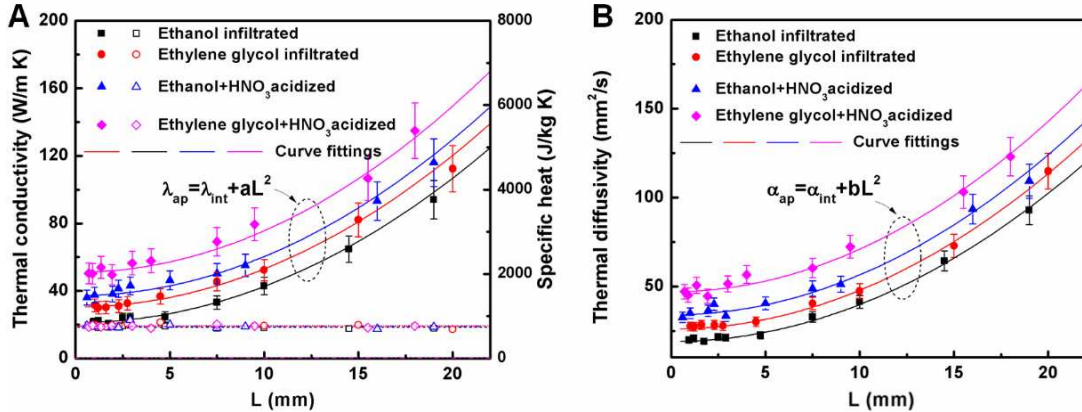


**Fig. 8. Distance dependence of the  $\kappa_{ap}$  (A) and  $\alpha_{ap}$  (B) of CNTF-E-I, CNTF-EG-I, CNTF-E-I-A and CNTF-EG-I-A samples measured by self-heating  $3\omega$  method. Solid lines are simulated by Eqs. (6) and (7), respectively. Fitting parameters are shown in Table 1. Heat capacity extracted from measured  $\kappa(L)$  and  $\alpha(L)$  shown by open squares, circles, triangles and rhombuses. Dashed lines are the average values for specific heat.**

The quadratic dependence on length for apparent thermal transport phenomenon for functionalized CNT fibers is observed and quantitatively described in Table 1 (Column  $\alpha_{ap}$  and  $\kappa_{ap}$ ). This accurate quadratic dependence, owing to radial radiation heat loss, enables CNT fibers a unique length programmed thermal transport performance. In addition, distinguishable thermal conductivity and thermal diffusivity for the four densified and functionalized samples (shown in Fig. 8) presage that some microscopic structure variations definitely play an important role in heat transport mechanism. Since the thermal conductivity in CVD grown MWCNTs is mainly thought of as arising from defects which can reduce their intrinsic thermal conductivity combined with inter-tube interfacial resistance [[31]] and our Raman results show the increase in defect concentration after moderate acidization was unobvious, inter-tube interfacial resistance play a significant role in determining the resultant thermal conductivity of CNT fiber. This effect is generally quantitatively described by the reciprocal of the inter-tube interfacial resistance, i.e.

the inter-bundle interfacial thermal conductance,  $G_t$ , whose magnitude has been verified to be strongly dependent on CNT spacing, contact area and inter-tube interaction [[58], [59]]. Our physical and chemical manipulation were concerned about modifying these parameters for the inter-bundle interface. Raman results have verified our manipulations have no effect on increasing bundle contact length or bundle contact area. However, local densification (Coulomb electrostatic cohesion) would produce stronger inter-tube interaction and narrower spacing for adjacent CNT bundles at the contact sites compared with non-densification CNTF, resulting in an increased inter-bundle interfacial thermal conductance [[37]]. This occurs because of two aspects of reasons: (1) the van der Waals interactions, which provide the main heat transfer mechanism between the physically manipulated nanotubes fibers, i.e. CNTF-E-I and CNTF-EG-I, are weakened with increasing distance. 2) Weak attractive binding interaction between neighbouring CNTs induced by dipole moments of highly polar solvents also contributes to the increased interface conductance. For chemically manipulated fibers, i.e. CNTF-E-I-A and CNTF-EG-I-A, the extra short, covalently bonding functional groups tend to form stronger inter-bundle interactions than the van der Waals forces, which further improves the interface conductance.

To gain insight into the electrical and thermal transport in CNT fibers with manipulated inter-bundle interfaces, we analysed their microscopic assembly structures and the corresponding thermal and electrical network model, as sketched in Fig. 9. An individual CNT (marked in dotted lines) with length  $l \sim 260 \mu\text{m}$  [[35]] is helix-wound along the axial direction of the CNT fiber at helix angle ( $90^\circ - \theta$ ). A bundle of CNTs with the same length could be considered as a periodic unit of the investigated CNT fiber. CNTs in one bundle were “head-to-tail” in line with those in the next bundle, and the CNT bundles perform as parallel transport channels which

contribute together to the axial thermal transport. As it has been confirmed that the junctions formed between MWCNTs belonging to different bundles do not appreciably diminish the phonon transmission along the same CNT [[60]], the temperature on the contact section of each involved CNT bundle can be considered constant. Consequently the temperature drops exist only at the inter-bundle interfaces for the bundle-bundle contact section. The axial thermal current  $J$  is successively along the individual CNT bundles in Unit N and the inter-bundle interface then the CNT bundles in Unit N+1. Within a Unit with length  $l$ , the total thermal resistance is described as

$$\langle |\Delta T| \rangle / J = \left( \frac{1}{\kappa_{\text{CNT}} (A d L_t)} + \frac{1}{G_c} \right) / \left( \frac{\pi D^2 / 4}{A \pi d^2 / 4} B \right) \quad (8)$$

where  $\langle |\Delta T| \rangle$  is the absolute average temperature drop for a unit,  $\kappa_{\text{CNT}}$  is the thermal conductivity of an individual CNT bundle and has been experimentally validated to be 2000 W/mK for very small bundles typically comprising of 2 or 3 MWCNTs [64], [65],  $d$  is the average CNT diameter,  $G_c$  is a universal symbol representing the inter-bundle interface conductance, which equals to  $G_t$  for thermal transport and  $G_e$  for electrical transport,  $A$  is the average number of tubes in each bundle which has been calculated according to statistical distribution of bundle size, i.e. 1~2 for ethanol treated samples and approximately 3 for ethylene glycol treated samples, and  $B$  is the fraction of successful contact for contiguous bundles on a cross-section.  $B$  has large uncertainty since it is hard to figure out the accurate number of dangling CNT ends, loops and misalignment of nanotubes. According to the experimentally obtained thermal conductivity, the total thermal resistance of a fiber unit can be calculated as

$$\langle |\Delta T| \rangle / J = \frac{1}{\kappa_L \pi D^2 / 4} \quad (9)$$

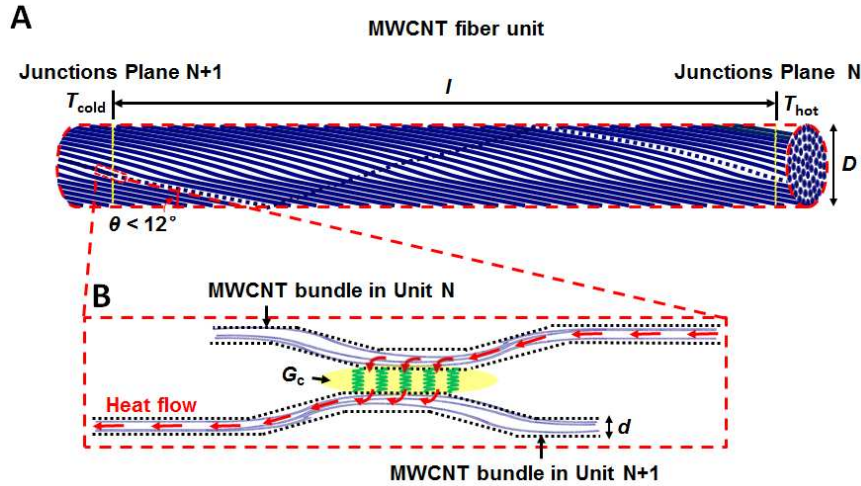


**Fig. 9.** Schematic for (A) microscopic surface structure of CNT fiber assembled by individual CNTs. (B) enlarged inter-bundle interface structure and heat flow from bundle in Unit N to bundle in Unit N+1 via finite inter-tube interface conductance  $G_c$ .

Combined with Eqs. (8)-(9) and the known data listed in Table 1, the inter-bundle interface thermal conductance  $G_t$  and interface electrical conductance  $G_e$  were deduced. According to the calculation, the most important factor determining electrical and thermal transport in CNT ensembles is still believed to be  $G_c$  [[60]-[63]] even though the CNTs is up to 260  $\mu\text{m}$  long. It is to be noted that the large uncertainties of deduced values for  $G_e$  and  $G_t$  stem from the uncertainty of the value of B. However, the value of B for the four fibers should be almost the same as the fabrication process and conditions are identical. Therefore, the evolution trends for  $G_e$  and  $G_t$  are still credible even if the magnitude could be smaller in the case of more failure of inter-tube connections. Clearly from the estimated results for  $G_e$  and  $G_t$  summarized in Table 2, the inter-bundle interface electrical and thermal conductance are greatly enhanced via physical infiltration and short covalently bonding linkers. More significantly, by comparing the inter-bundle interfacial thermal and electrical conductance for the four functionalized samples, we can clearly discern their programmable potential, as sketched in Fig. 10. Local densification induced by

polar protic liquid infiltration encourages individual CNTs to form larger bundles which can remarkably bring about two benefits for the enhancement of the overall transport: shortening the spacing for adjacent CNT bundles at the contact sites (shown in Fig. 9) and introducing additional Coulomb electrostatic interaction between neighbouring CNTs induced by dipole moments of highly polar solvents, which finally result in a nearly 2.8 times of enhancement in contact conductance, and reducing the number of inter-bundle contact interfaces. Chemical HNO<sub>3</sub> acidization directly contributes to improving the inter-bundle thermal and electrical conductance. In contrast to the conventional conception that oxidative acid treatment decrease the conductivity by deteriorating π-π conjugation structure in CNTs by creating some vacancy defects, theoretical [[64], [65]] and experimental [[66]] results have verified that the formation of vacancy defect-functional group pairs (VFPs) actually represents a tremendous improvement in the inter-tube conductance. For electrical transport, VFPs enable the original dangling bond to be perfectly saturated by the functional group and thus the defect band substantially shifts down to the Fermi level, which finally cause the system to be transformed from p-type semiconducting behavior to metal-like conducting behavior. For thermal transport, the stronger covalent bond in VFPs, compared with weak wan der Waals interaction, is indeed favorable to transferring thermal vibrations. Although the vacancy defect also performs as phonon scattering sites blocking vibration transport, this effect is limited and finally the advantage of VFPs dominates the thermal transport. This different electrical and thermal transport mechanism are rigidly reflected by the differentiated improvement magnitude of inter-bundle electrical and thermal conductance, i.e. about 75% and 95% improvement for thermal and electrical contact conductance, respectively. It is to be noted that physical and chemical operations, i.e. densification and functionalization, render synergistic effect of enhancing the electrical and

thermal conductivities of CNTFs. Quantitatively controllable operation of inter-bundle contact conductance could be realized based on the above discussions. Specifically, physical densification performs like a multiplication operator ( $\sim 2.8\times$  multiplication using ethylene glycol to replace ethanol) and chemical acidization an addition operator (about 75% elevation for inter-bundle thermal contact conductance and 95% for inter-bundle electrical contact conductance). Therefore, we can envisage that programmable potential for electrical and thermal transport of CNT ensembles could be realized through proper physical densification and chemical functionalization manipulations. It is important to note that this programmable operation of unique electrical and thermal properties at inter-bundle interfaces allow us to exquisitely elevate the inter-bundle interfacial electrical and thermal conductance of the CNT fibers in order to attain enhanced electrical and thermal conductivity.

**Table 2. Predicated Inter-bundle Interfacial Thermal Conductance  $G_t$ , Inter-bundle Interfacial Electrical Conductance  $G_e$  for Functionalized and Condensed CNT Fibers.**

Sample	l [μm]	d [nm]	A	B	$\kappa_{\text{CNT}}$ [W/mK]	$\sigma_{\text{CNT}}$ [S/m]	$G_t$ [pW/K]	$G_e$ [/GΩ]
CNTF-E-I	260	5.8 <sup>a</sup>	1~2	< 1	$\sim 2000^b$	$\sim 1.3\times 10^{6c}$	3.2	3.7
CNTF-EG-I	260	5.8 <sup>a</sup>	3	< 1	$\sim 2000^b$	$\sim 1.3\times 10^{6c}$	9.2	9.4
CNTF-E-I-A	260	5.8 <sup>a</sup>	1~2	< 1	$\sim 2000^b$	$\sim 1.3\times 10^{6c}$	5.6	7.2

CNTF-EG-I-A	260	5.8 <sup>a</sup>	3	< 1	$\sim 2000^b$	$\sim 1.3 \times 10^6^c$	15.4	20.1
-------------	-----	------------------	---	-----	---------------	--------------------------	------	------

<sup>a</sup> characterized by TEM and reported in Ref. [[37]].

<sup>b</sup> see Ref. [[64], [65]].

<sup>c</sup> see Ref. [[66]].

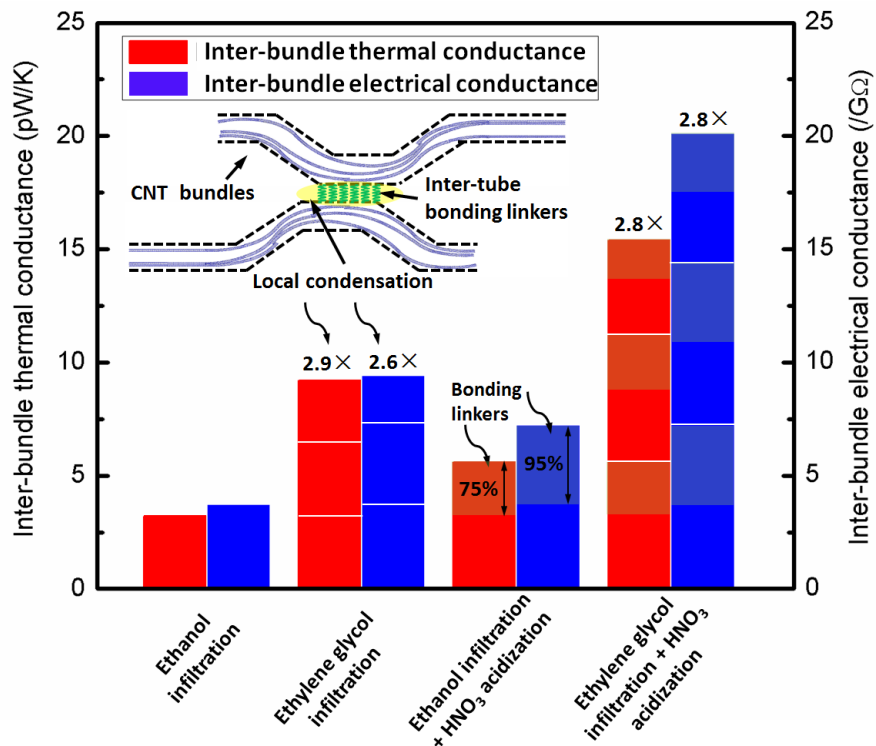


**Fig. 10. Programmable inter-bundle interface thermal and electrical conductance for four functionalized and condensed CNT fibers.**

#### 4. Conclusions

In summary, we proposed a programmable functionalization and densification manipulation scheme for improving the thermal and electrical transport of CNT assembled fibers. The manipulation scheme includes: i) length programmed apparent thermal conductivity and thermal diffusivity of CNT fibers based on accurate quadratic equations, summarized in

**Table 1**; ii) temperature programmed RT electrical conductivity of CNT fibers based on FIT mechanism, listed in [Fig. 7](#); and iii) nanoscale structure programmed inter-bundle electrical and thermal contact conductance, sketched in [Fig. 10](#). The first scheme is based on the rigid quadratic dependence of radiation heat loss on fiber length, and the second is according to the decisive effect of temperature-induced thermal fluctuation on the success probability of electron tunneling. The third is on the basis that inter-bundle interface conductance dominates the electrical and thermal transport in CNT assemblies, believed to be the most intricate but effective tuning approach. Creating local densification and short covalently bonding linkers between contiguous bundles are proved effective for realizing nanoscale structure variations. Local densification induced through polar protic liquid infiltration contributes to stronger inter-tube interaction and narrower inter-bundle spacing at the contact sites compared with non-densification CNTF, which performs like a multiplication operator for inter-bundle electrical and thermal contact conductance. VFPs created through short-time concentrated HNO<sub>3</sub> acidization substantially shift down the defect band to the Fermi level and provide strong covalent bond favorable to transferring thermal vibrations, which works like an addition operator for inter-bundle electrical and thermal contact conductance. Our finding that the electrical and thermal transport of CNT fibers have programmable operation potential will guide future development of controllable CNT-based thermal and electrical management nanodevices in energy conservation and conversion, information technology and medical therapy.

## Acknowledgements

This research receives financial support from Projects 51306183 and 51336009 supported by National Natural Science Foundation of China (NSFC) and National Basic Research Program of

China (Grant No. 2012CB933200). Lin Qiu and Xinghua Zheng also thank the support from the China Scholarship Council (Grant No. 201404910084 and 201404910085).

## REFERENCES

- [1] Cahill DG, Braun PV, Chen G, Clarke DR, Fan S, Goodson, KE, et al. Nanoscale thermal transport. II. 2003-2012. *Appl Phys Rev* 2014;1(1):011305.
- [2] Wen DS. Nanoparticle-related heat transfer phenomenon and its application in biomedical fields. *Heat Transfer Eng* 2013;34(14):1171–9.
- [3] Lee WJ, Ramasamy E, Lee DY, Song JS. Efficient dye-sensitized solar cells with catalytic multiwall carbon nanotube counter electrodes. *ACS Appl Mater Interfaces* 2009;1(6):1145–9.
- [4] Xiong F, Bae MH, Dai Y, Liao AD, Behnam A, Carrion EA, et al. Self-aligned nanotube–nanowire phase change memory. *Nano Lett* 2013;13(2):464–9.
- [5] Amin M, Stringer J. The electric power grid: today and tomorrow. *MRS Bull* 2008;33(4):399-407.
- [6] Ericson LM, Fan H, Peng H, Davis VA, Zhou W, Sulpizio J, et al. Macroscopic, neat, single-walled carbon nanotube fibres. *Science* 2004;305(5689):1447–50.
- [7] Qi P, Vermesh O, Grecu M, Javey A, Wang Q, Dai H, et al. Toward large arrays of multiplex functionalized carbon nanotube sensors for highly sensitive and selective molecular detection. *Nano Lett* 2003;3(3):347–51.
- [8] Kostarelos K. The long and short of carbon nanotube toxicity. *Nat Biotechnol* 2008;26:774–6.
- [9] Behabtu N, Young CC, Tsentalovich DE, Kleinerman O, Wang X, Ma, AWK, et al. Strong, light, multifunctional fibres of carbon nanotubes with ultrahigh conductivity. *Science* 2013;339(6116):182–6.
- [10] Jarosz PR, Schauerman C, Alvarenga J, Moses B, Mastrangelo T, Raffaelle R, et al. Carbon nanotube wires and cables: Near-term applications and future perspectives. *Nanoscale* 2011;3(11):4542–53.
- [11] Mintmire JW, Dunlap BI, White CT. Are fullerene tubules metallic? *Phys Rev Lett* 1992;68(5):631–4.

- [12] Hamada N, Sawada A, Oshiyama A. New one-dimensional conductors: graphitic microtubules. *Phys Rev Lett* 1992;68(10):1579–81.
- [13] Berber S, Kwon YK, Tomanek D. Unusually high thermal conductivity of carbon nanotubes. *Phys Rev Lett* 2000;84(20):4613–6.
- [14] Che J, Cagin T, Goddard III WA. Thermal conductivity of carbon nanotubes. *Nanotechnol* 2000;11:65–9.
- [15] Ebbesen TW, Lezec HJ, Hiura H, Bennett JW, Ghaemi HF, Thio T. Electrical conductivity of individual carbon nanotubes. *Nature* 1996;382(6586):54–6.
- [16] Bachtold A, Henny M, Terrier C, Strunk C, Forro L. Contacting carbon nanotubes selectively with low-ohmic contacts for four-probe electric measurements. *Appl Phys Lett* 1998;73(2):274–6.
- [17] McEuen PL, Fuhrer M, Park H. Single-walled carbon nanotube electronics. *IEEE Trans Nanotechnol* 2002;1(1):78–85.
- [18] Gao B, Chen YF, Fuhrer MS, Glattli DC, Bachtold A. Four-point resistance of individual single-wall carbon nanotubes. *Phys Rev Lett* 2005;95(19):196802.
- [19] Pop E, Mann D, Wang Q, Goodson KE, Dai H. Thermal conductance of an individual single-wall carbon nanotube above room temperature. *Nano Lett* 2006;6(1):96–100.
- [20] Li Q, Liu C, Wang X, Fan S. Measuring the thermal conductivity of individual carbon nanotubes by the Raman shift method. *Nanotechnol* 2009;20(14):145702.
- [21] Yu C, Shi L, Yao Z, Li D, Majumdar A. Thermal conductance and thermopower of an individual single-wall carbon nanotube. *Nano Lett* 2005;5(9):1842–6.
- [22] Fujii M, Zhang X, Xie H, Ago H, Takahashi K, Ikuta T, et al. Measuring the thermal conductivity of a single carbon nanotube. *Phys Rev Lett* 2005;95(6):065502.
- [23] Wang ZL, Tang DW, Li XB, Zheng XH, Zhang WG, Zheng LX, et al. Length-dependent thermal conductivity of an individual single-wall carbon nanotube. *Appl Phys Lett* 2007;91(12):123119.
- [24] Marconnet AM, Panzer MA, Goodson KE. Thermal conduction phenomena in carbon nanotubes and related nanostructured materials. *Rev Mod Phys* 2013;85(3):1295–326.

- [25] Zhang M, Atkinson KR, Baughman RH. Multifunctional carbon nanotube yarns by downsizing an ancient technology. *Science* 2004;306(5700):1358–61.
- [26] Zhu HW, Xu L, Wu D, Wei BQ, Vajtai R, Ajayan PM. Direct synthesis of long single-walled carbon nanotube strands. *Science* 2002;296(5569):884–6.
- [27] Aliev AE, Guthy C, Zhang M, Fang S, Zakhidov AA, Fischer JE, et al. Thermal transport in MWCNT sheets and yarns. *Carbon* 2007;45(15):2880–8.
- [28] Jakubinek MB, Johnson MB, White MA, Jayasinghe C, Li G, Cho W, et al. Thermal and electrical conductivity of array-spun multi-walled carbon nanotube yarns. *Carbon* 2012;50(1):244–8.
- [29] Kingston CT, Martínez-Rubí Y, Guan J, Barnes M, Scriven C, Sturgeon RE, et al. Coupled thermogravimetry, mass spectrometry, and infrared spectroscopy for quantification of surface functionality on single-walled carbon nanotubes. *Anal Bioanal Chem* 2010;396(3):1037–44.
- [30] Nirmalraj PN, Lyons PE, De S, Coleman JN, Boland JJ. Electrical connectivity in single-walled carbon nanotube networks. *Nano Lett* 2009;9(11):3890–5.
- [31] Prasher RS, Hu XJ, Chalopin Y, Mingo N, Lofgreen K, Volz S, et al. Turning carbon nanotubes from exceptional heat conductors into insulators. *Phys Rev Lett* 2009;102(10):105901.
- [32] Li S, Zhang X, Zhao J, Meng F, Xu G, Yong Z, et al. Enhancement of carbon nanotube fibres using different solvents and polymers. *Compos Sci Technol* 2012;72(12):1402–7.
- [33] Jia J, Zhao J, Xu G, Di J, Yong Z, Tao Y, et al. A Comparison of the mechanical properties of fibres spun from different carbon nanotubes. *Carbon* 2011;49(4):1333–9.
- [34] Meng F, Zhang X, Li R, Zhao J, Xuan X, Wang X, et al. Electro-induced mechanical and thermal responses of carbon nanotube fibres. *Adv Mater* 2014;26(16):2480–5.
- [35] Meng FC, Zhao JN, Ye YT, Zhang XH, Li QW. Carbon nanotube fibres for electrochemical applications: Effect of enhanced interfaces by an acid treatment. *Nanoscale* 2012;4(23):7464–8.
- [36] Qiu L, Zheng XH, Zhu J, Su GP, Tang DW. The effect of grain size on the lattice thermal conductivity of an individual polyacrylonitrile-based carbon fibre. *Carbon* 2013;51:265–73.
- [37] Qiu J, Terrones J, Vilatela JJ, Vickers ME, Elliott JA, Windle AH. Liquid infiltration into carbon nanotube fibres: Effect on structure and electrical properties. *ASC Nano* 2013;7(10):8412–22.

- [38] Bergin SD, Nicolosi V, Streich PV, Giordani S, Sun Z, Windle AH, et al. Towards solutions of single-walled carbon nanotubes in common solvents. *Adv Mater* 2008;20(10):1876–81.
- [39] Hernandez Y, Nicolosi V, Lotya M, Blighe FM, Sun Z, De S, et al. High-yield production of graphene by liquid-phase exfoliation of graphite. *Nat Nanotechnol* 2008;3:563–8.
- [40] Kaur S, Raravikar N, Helms BA, Prasher R, Ogletree DF. Enhanced thermal transport at covalently functionalized carbon nanotube array interfaces. *Nat Commun* 2014;5:3082.
- [41] Iwashita N, Park, CR, Fujimoto H, Shiraishi M, Inagaki M. Specification for a standard procedure of X-ray diffraction measurements on carbon materials. *Carbon* 2004;42(4):701–14.
- [42] Nysten B, Issi JP, Barton JR, Boyington DR, Lavin JG. Determination of lattice defects in carbon fibres by means of thermal-conductivity measurements. *Phys Rev B* 1991;44(5):2142–8.
- [43] Kharissova OV, Kharisov BI. Variations of interlayer spacing in carbon nanotubes. *RSC Adv* 2014;4:30807–15.
- [44] Palser AHR. Interlayer interactions in graphite and carbon nanotubes. *Phys Chem Chem Phys* 1999;1:4459–64.
- [45] Delhaes P, Couzi M, Trinquecoste M, Dentzer J, Hamidou H, Vix-Guterl C. A comparison between Raman spectroscopy and surface characterizations of multiwall carbon nanotubes. *Carbon* 2006;44(14):3005–13.
- [46] Tuinstra F, Koenig JL. Characterization of graphite fibre surfaces with Raman spectroscopy. *J Compos Mater* 1970;4(4):492–9.
- [47] Matthews MJ, Pimenta MA, Dresselhaus G, Dresselhaus MS, Endo M. Origin of dispersive effects of the Raman D band in carbon materials. *Phys Rev B* 1999;59(10):R6585–8.
- [48] Barnes TM, Blackburn JL, van de Lagemaat J, Coutts TJ, Heben MJ. Reversibility, dopant desorption, and tunneling in the temperature dependent conductivity of type-separated, conductive carbon nanotube networks. *ACS Nano* 2008;2(9):1968–76.
- [49] Lu L, Yi W, Zhang DL.  $3\omega$  method for specific heat and thermal conductivity measurements. *Rev Sci Instrum* 2001;72(7):2996–3003.

- [50] Aliev AE, Lima MH, Silverman EM, Baughman RH. Thermal conductivity of multi-walled carbon nanotube sheets: Radiation losses and quenching of phonon modes. *Nanotechnol* 2010;21(3):035709.
- [51] Yi W, Lu L, Zhang DL, Pan ZW, Xie SS. Linear specific heat of carbon nanotubes. *Phys Rev B* 1999;59(14):R9015–8.
- [52] Li QW, Li Y, Zhang XF, Chikkannanavar SB, Zhao YH, Dangelewicz AM, et al. Structure-dependent electrical properties of carbon nanotube fibres. *Adv Mater* 2007;19(20):3358–63.
- [53] Ksenevich VK, Odzaev VB, Martunas Z, Seliuta D, Valusis G, Galibert J, et al. Localization and nonlinear transport in single walled carbon nanotube fibres. *J Appl Phys* 2008;104(7):073724.
- [54] Sheng P, Sichel EK, Gittleman JI. Fluctuation-induced tunneling conduction in carbon-polyvinylchloride composites. *Phys Rev Lett* 1978;40(18):1197–200.
- [55] Sheng P. Fluctuation-induced tunneling conduction in disordered materials. *Phys Rev B* 1980;21:2180–95.
- [56] Lai YR, Yu KF, Lin YH, Wu JC, Lin JJ. Observation of fluctuation-induced tunneling conduction in micrometer-sized tunnel junctions. *AIP Advances* 2012;2:032155.
- [57] Zhang X, Fujiwara S, Fujii M. Measurements of thermal conductivity and electrical conductivity of a single carbon fibre. *Int J Thermophys* 2000;21(4):965–980.
- [58] Zhong H, Lukes JR. Interfacial thermal resistance between carbon nanotubes: Molecular dynamics simulations and analytical thermal modeling. *Phys Rev B* 2006;74(12):125403.
- [59] Evans WJ, Shen M, Keblinski P. Inter-tube thermal conductance in carbon nanotubes arrays and bundles: Effects of contact area and pressure. *Appl Phys Lett* 2012;100(26):261908.
- [60] Chalopin Y, Volz S, Mingo N. Upper bound to the thermal conductivity of carbon nanotube pellets. *J Appl Phys* 2009;105(8):084301.
- [61] Balandin AA. Thermal properties of graphene and nanostructured carbon materials. *Nat Mater* 2011;10:569–81.
- [62] Kim P, Shi L, Majumdar A, McEuen PL. Thermal transport measurements of individual multiwalled nanotubes. *Phys Rev Lett* 2001;87(21):215502.

- [63] Fuhrer MS, Nygård J, Shih L, Forero M, Yoon YG, Mazzoni MSC, et al. Crossed nanotube junctions. *Science* 2000;288(5465):494–7.
- [64] Burghard M. Electronic and vibrational properties of chemically modified single-wall carbon nanotubes. *Surf Sci Rep* 2005;58(1-4):1–109.
- [65] Wang C, Zhou G, Wu J, Gu BL, Duan W. Effects of vacancy-carboxyl pair functionalization on electronic properties of carbon nanotubes. *Appl Phys Lett* 2006;89(17):173130.
- [66] Tantang H, Ong JY, Loh CL, Dong X, Chen P, Chen Y, et al. Using oxidation to increase the electrical conductivity of carbon nanotube electrodes. *Carbon* 2009;47(7):1867–70.